CrystEngComm

Ligand Geometry Directs the Packing and Symmetry of One-Dimensional Helical Motifs in Lead Oxide Naphthoates and Biphenylcarboxylates

Journal:	*CrystEngComm*
Manuscript ID	CE-ART-08-2020-001150.R1
Article Type:	Paper
Date Submitted by the Author:	08-Sep-2020
Complete List of Authors:	Hammer, Arden; Oberlin College, Department of Chemistry and Biochemistry Jia, Xiwen; Haverford College, Department of Chemistry Zeller, Matthias; Purdue University, Department of Chemistry Coughlin, Ezra; Purdue University, Chemistry Zhang, Weiguo; University of Houston, Chemistry Department Oertel, Catherine; Oberlin College, Department of Chemistry and Biochemistry

ARTICLE

Ligand Geometry Directs the Packing and Symmetry of One-Dimensional Helical Motifs in Lead Oxide Naphthoates and Biphenylcarboxylates

Received 00th January 20xx,
Accepted 00th January 20xx

DOI: 10.1039/x0xx00000x

Arden C. Hammer,[a] Xiwen Jia,[b] Matthias Zeller,[c] Ezra J. Coughlin,[c] Weiguo Zhang,[d] and Catherine M. Oertel*[a]

Extended inorganic hybrids are highly tunable, with changes in the identity of each component giving rise to a variety of different architectures and symmetries. Lead oxide carboxylates are a family of extended inorganic hybrids in which inorganic substructures based on edge-sharing Pb_4O tetrahedra are further coordinated by carboxylate ligands. It has previously been shown that the dimensionality of these compounds correlates with the noncoordinating to coordinating volume ratio of the organic ligand. Here, we present five novel lead oxide carboxylates – two with isomeric naphthoate ligands and three with isomeric biphenylcarboxylate ligands – in order to address the role of ligand geometry in directing the spatial arrangement and symmetry of inorganic motifs in these compounds. The compounds have been characterized by single crystal X-ray diffraction, powder X-ray diffraction, thermogravimetric analysis, and elemental analysis. In these compounds, the spatial arrangement of helical inorganic chains is controlled by the extent to which ligands on a given chain fill space immediately surrounding that chain. Noncovalent interaction index calculations have been undertaken for the naphthoate compounds in order to visualize the role of aromatic-aromatic interactions in stabilizing the structures. The structural patterns found here may be applicable to other hybrid systems containing one-dimensional, extended inorganic substructures.

Introduction

Extended inorganic hybrids are inorganic-organic hybrid materials in which metal atoms are bridged by single atoms infinitely in one or more dimensions, forming extended inorganic substructures.[1] These linking atoms may be single-atom anions or donor atoms on organic ligands. Ligands may additionally complete the metal atoms' coordination spheres or create connectivity between inorganic units. In other cases, organic cations provide charge balance and space filling. The presence of inorganic substructures with extended M-X-M (X = O, S, halide) linkages can result in magnetic, optical, and ferroelectric properties more typical of purely inorganic materials.[2-9] At the same time, the organic component influences the extent of condensation, topology, spatial arrangement, and symmetry of the inorganic phase.[10-13] The structural anisotropy of different bond types in different dimensions can lead to anisotropy of mechanical properties and ability to exfoliate compounds into nanomaterials with well-defined architectures.[14,15] The structural diversity of this type of compound is a strength, but strategies are needed for interpreting and predicting the structures that arise from a particular set of building blocks. For example, for the specific family of hybrid perovskite-like halides, tolerance factor approaches have been pursued in predicting the inorganic dimensionalities likely to occur with a given organic cation.[16-18] However, there is an opportunity to develop strategies that focus on other families of compounds or that take into account ligand characteristics other than size.

Lead oxide carboxylates are extended inorganic hybrids that form from reactions between PbO and carboxylic acids.[19] The common building blocks in these compounds are oxygen-centered Pb_4O tetrahedra that share edges to form extended substructures. The condensation of these inorganic motifs differs for different organic ligands. Structures containing Pb_2O^{2+} single chains, $Pb_3O_2^{2+}$ double chains, and $Pb_4O_3^{2+}$ triple chains have all been observed, with remaining coordination sites on the lead atoms filled by oxygen atoms on the organic ligands.[20,21] There is also variety in the symmetries of the inorganic substructures. Lead oxide formate, $Pb_2O(CHOO)_2$, contains linear Pb_2O^{2+} chains, while in several compounds with functionalized benzoate ligands, $Pb_2O(C_7H_4O_2X)_2$ (X = H, Br, CH_3) and $Pb_2O(C_6H_4NO_2)_2$, the Pb_2O^{2+} motifs are helical.[19,21-23] The spatial relationship between inorganic motifs in these

[a] Department of Chemistry and Biochemistry, Oberlin College, 119 Woodland Street, Oberlin, OH 44074, United States
[b] Department of Chemistry, Haverford College, 370 Lancaster Avenue, Haverford, PA 19041, United States
[c] Department of Chemistry, Purdue University, 560 Oval Drive, West Lafayette, IN 47907, United States
[d] Department of Chemistry, University of Houston, Houston, TX 77204-5003, United States

Electronic Supplementary Information (ESI) available: thermal ellipsoid figures; powder X-ray diffraction patterns; thermogravimetric analysis traces; illustrations of lead(II) coordination environments; bond valence sums for lead(II) sites; crystallographic data at CCDC 1967357-1967361. See DOI: 10.1039/x0xx00000x

structures, including whether or not they are related to each other by inversion, also varies with the identity of the organic ligand.

Previous work on lead oxide carboxylates has shown that the dimensionality of these compounds is correlated with the noncoordinating to coordinating volume ratio of the organic ligand.[21] Carboxylate ligands with large noncoordinating volumes compared with the volume of the coordinating oxygen atoms gave rise to one-dimensional structures, while ligands with the smallest volume ratios produced three-dimensional structures. However, the effect of changing the spatial distribution of noncoordinating volume with respect to the coordinating groups on the ligands has not been systematically examined. In order to further probe the role of ligand shape in the current study, we selected two isomeric pairs of carboxylate ligands that have nearly identical noncoordinating to coordinating volume ratios and chemical functionalities but different noncoordinating volume geometries (Figure 1). We have synthesized and structurally characterized five novel lead oxide carboxylates: lead oxide 1-naphthoate (**1**), lead oxide 2-naphthoate hydrate (**2**), two polymorphs of lead oxide biphenyl-2-carboxylate (**3** and **4**), and lead oxide biphenyl-3-carboxylate (**5**).

Despite having in common chiral one-dimensional inorganic substructures that are coordinated by carboxylate ligands, the new compounds have different global symmetries. In our analysis, we have compared how the ligands fill space around their respective inorganic cores and the extent to which ligands associated with different inorganic chains interdigitate. In turn, we have considered how these factors affect the overall packing patterns. Noncovalent interaction (NCI) index calculations have recently been used to identify and visualize weaker interactions in hybrid inorganic-organic materials.[24-26] Here, we have used this method to analyze the structures of **1** and **2** with a particular interest in determining the role of aromatic-aromatic interactions in stabilizing these compounds. This has made it possible to identify structural influences beyond those of space filling requirements.

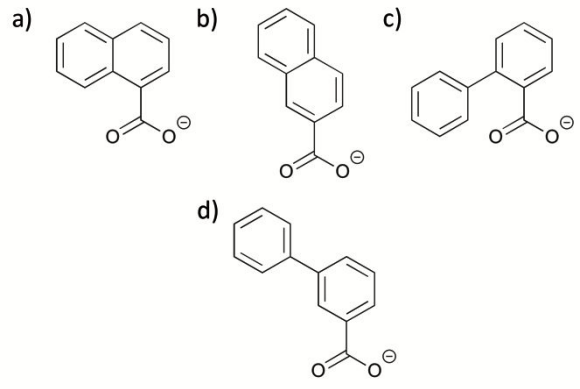

Figure 1. Carboxylate ligands selected for study: a) 1-naphthoate, b) 2-naphthoate, c) biphenyl-2-carboxylate, d) biphenyl-3-carboxylate

Experimental

Materials. PbO (99%, Aldrich), 1-naphthoic acid (96%, Aldrich), 2-naphthoic acid (98%, Aldrich), biphenyl-2-carboxylic acid (98% Aldrich), and biphenyl-3-carboxylic acid (97%, Aldrich) were used as received. ACS grade 200 proof ethyl alcohol (Aldrich), ACS grade 99% isopropyl alcohol (Aldrich), certified grade 2-propanol (Fisher), and deionized water were used as solvents without further purification. For each reaction, solid reactants were co-ground in an agate mortar and pestle before being combined with the solvent. Reactions were carried out in 23 mL Teflon cups sealed in stainless steel autoclaves (Parr).

Instrumentation. Powder X-ray diffraction (PXRD) was conducted at ambient temperature on a Rigaku Ultima IV diffractometer with Cu K_α radiation. Scans were collected from 3° to 50° 2θ at 0.50°/min. All samples were ground with an agate mortar and pestle prior to analysis by PXRD. Thermogravimetric analysis (TGA) was conducted under air (50 mL/min) using a Mettler-Toledo TGA/DSC 1 STARe System. Samples were heated in alumina crucibles from 30 °C to 600 °C at 10 °C/min. Elemental analysis was conducted by Micro Analysis, Inc., Wilmington, DE.

Measurement of Second Harmonic Generation. Second harmonic generation (SHG) activity was measured for a polycrystalline sample using a modified Kurtz-NLO system with a 1064 nm pulsed Nd:YAG laser.[27] Light was collected in reflection mode and detected with a photomultiplier tube equipped with a 532 nm narrow-band-pass filter. The intensity of 532 nm light was compared with that generated by a standard sample of polycrystalline α-SiO_2.

Synthesis of 1. To obtain single crystals of **1**, PbO (0.446 g, 2 mmol) and 1-naphthoic acid (0.344 g, 2 mmol) were combined with isopropanol (3 mL) and deionized water (7 mL). The sealed reaction vessel was heated to 180 °C at 5 °C/min, held at 180 °C for 24 h, and cooled to ambient temperature at 0.1 °C/min. The product mixture contained clear, acicular crystals with a faint yellow cast, which were removed for single-crystal diffraction experiments.

To obtain a phase-pure sample of **1**, PbO (0.223 g, 1 mmol) and 1-naphthoic acid (0.172 g, 1 mmol) were transferred to a glass culture tube with ethanol (8 mL) and deionized water (2 mL). The resulting slurry was sonicated for 20 min, transferred to a 23 mL Teflon cup, and sparged with nitrogen gas for 15 min. The mixture was heated to 200 °C at 5 °C/min, held at 200 °C for 24 h, and cooled to ambient temperature at 0.1 °C/min. The product mixture contained clear and colorless, acicular crystals. The crystals were collected by suction filtration through a Hirsch funnel (1 mm pore diameter) without filter paper and rinsed with ethanol (40 x 1 mL). The product was dried in air and phase purity confirmed by PXRD (Figure S6, ESI). Yield: 0.243 g (63%). Predicted (found) for $C_{22}H_{14}O_5Pb_2$: C 34.20% (34.05%), H 1.82% (1.86%).

Synthesis of 2. To obtain single crystals of **2**, PbO (0.446 g, 2 mmol) and 2-naphthoic acid (0.344 g, 2 mmol) were combined with isopropanol (5 mL) and deionized water (5 mL). The sealed reaction vessel was heated to 180 °C at 5 °C/min, held at 180 °C for 24 h, and cooled to ambient temperature at 0.1 °C/min. The

product mixture contained clear, acicular crystals having a faint yellow cast, which were removed for diffraction experiments. The solution had a yellow cast and also contained a second colorless, crystalline phase with a plate-like habit.

A nearly phase-pure powder of **2** was prepared by combining PbO (0.223 g, 1 mmol) and 2-naphthoic acid (0.172 g, 1 mmol) with 10 drops of ethanol. The sealed reaction vessel was heated to 180 °C at 5 °C/min, held at 180 °C for 24 h, and cooled to ambient temperature at 0.1 °C/min. This yielded a white powder that required no further drying. Phase purity was evaluated via PXRD (Figure S7, ESI). Yield: 0.310 g (80%). Predicted (found) for $C_{22}H_{14}O_5Pb_2 \cdot 0.16H_2O$: C 34.07% (33.70%), H 1.86% (1.97%).

Synthesis of 3. To obtain single crystals of **3**, PbO (0.112 g, 0.5 mmol) and biphenyl-2-carboxylic acid (0.099 g, 0.5 mmol) were combined with isopropanol (8 mL) and deionized water (2 mL). The sealed reaction vessel was placed in a furnace at 200 °C, which immediately began cooling to ambient temperature at a rate of 0.01 °C/min. The product mixture contained clear and colorless, acicular crystals, which were removed for diffraction experiments.

To obtain a phase-pure sample of **3**, PbO (0.223 g, 1 mmol) and biphenyl-2-carboxylic acid (0.198 g, 1 mmol) were combined with isopropanol (8 mL) and deionized water (2 mL). The sealed reaction vessel was heated to 180 °C at 5 °C/min, held at 180 °C for 24 h, and cooled to ambient temperature at 0.1 °C/min. The product mixture contained clear and colorless, acicular crystals. The crystals were collected by suction filtration through a Hirsch funnel (1 mm pore diameter) without filter paper and rinsed with ethanol (40 x 1 mL). The product was dried in air and phase purity confirmed by PXRD (Figure S8, ESI). Yield: 0.195 g (47%). Predicted (found) for $C_{26}H_{18}O_5Pb_2$: C 37.86% (37.66%), H 2.20% (2.11%).

Synthesis of 4. Compound **4** was prepared by combining PbO (0.223 g, 1 mmol) and biphenyl-2-carboxylic acid (0.198 g, 1 mmol) with isopropanol (5 mL) and deionized water (5 mL) in a glass culture tube. The resulting slurry was sonicated for 20 min, transferred to a 23 mL Teflon cup, and sparged with nitrogen gas for 15 min. The Teflon cup containing the reaction mixture was sealed in a stainless steel autoclave and placed in a furnace, where it was heated to 200 °C at 5 °C/min, held at 200 °C for 24 h, and cooled to ambient temperature at 0.01 °C/min. The product mixture contained clear and colorless, acicular crystals, some of which were set aside for single-crystal diffraction experiments. A bulk sample was isolated by suction filtration through a Hirsch funnel (1 mm pore diameter) without filter paper and rinsed with ethanol (40 x 1 mL). The product was dried in air and phase purity confirmed by PXRD (Figure S9, ESI). Yield: 0.280 g (68%). Predicted (found) for $C_{26}H_{18}O_5Pb_2$: C 37.86% (37.52%), H 2.20% (2.16%).

Synthesis of 5. To obtain single crystals of **5**, PbO (0.112 g, 0.5 mmol) and biphenyl-3-carboxylic acid (0.099 g, 0.5 mmol) were combined with isopropanol (8 mL) and deionized water (2 mL). The sealed reaction vessel was heated to 220 °C at 5 °C/min, held at 220 °C for 24 h, and cooled to ambient temperature at 0.01 °C/min. The product mixture contained clear and colorless, acicular crystals, which were removed for diffraction experiments.

To obtain a phase-pure sample of **5**, PbO (0.223 g, 1 mmol) and biphenyl-3-carboxylic acid (0.198 g, 1 mmol) were combined with isopropanol (5 mL) and deionized water (5 mL) in a glass culture tube. The resulting slurry was sonicated for 20 min, transferred to a 23 mL Teflon cup, and sparged with nitrogen gas for 15 min. The sealed reaction vessel was heated to 200 °C at 5 °C/min, held at 200 °C for 24 h, and cooled to ambient temperature at 0.01 °C/min. The product mixture contained clear and colorless, acicular crystals. The crystals were collected by suction filtration through a Hirsch funnel (1 mm pore diameter) without filter paper and rinsed with ethanol (1 x 40 mL). The product was dried in air and phase purity confirmed by PXRD (Figure S10, ESI). Yield: 0.208 g (50%). Predicted (found) for $C_{26}H_{18}O_5Pb_2$: C 37.86% (37.63%), H 2.20% (2.05%).

Crystal Structure Determination. Single-crystal X-ray diffraction was performed on a Bruker AXS D8 QUEST CMOS diffractometer. Data were collected at 150 K for **1**-**4** and at 296 K for **5**, which underwent a destructive phase change upon cooling. Experiments for **1**-**3** and **5** were carried out with sealed tube Mo Kα radiation, while microsource Cu Kα radiation was used for **4** because of small crystal size. Apex 3 was employed to determine initial unit cells and carry out data collection.[28] Data integration and unit cell determination were performed using SAINT.[29] Absorption corrections were applied using SADABS.[30] The structures were solved using direct methods and refined by full-matrix least-squares on F_o^2.[31] All non-hydrogen atoms were refined anisotropically. Refinement was completed with hydrogen atoms constrained to ride on carrying atoms. Refinement data for **1**-**5** are shown in Table 1.

Table 1. Refinement data for compounds **1**-**5**.

	1	**2**	**3**	**4**	**5**
empirical formula	$C_{22}H_{14}O_5Pb_2$	$C_{22}H_{14.31}O_{5.16}Pb_2$	$C_{26}H_{18}O_5Pb_2$	$C_{26}H_{18}O_5Pb_2$	$C_{26}H_{18}O_5Pb_2$
formula weight	772.71	775.55	824.78	824.78	824.78
wavelength (Å)	0.71073	0.71073	0.71073	1.54178	0.71073
temperature (K)	150(2)	150(2)	150(2)	150(2)	296(2)
crystal system	tetragonal	monoclinic	monoclinic	monoclinic	tetragonal
space group	$I4_1/a$	$C2/c$	$P2_1/c$	$P2_1/c$	$P4_1$
a (Å)	27.1581(11)	35.3686(18)	11.0324(8)	30.3539(11)	21.255(3)
b (Å)		10.8690(5)	50.385(4)	10.9884(4)	
c (Å)	10.8428(5)	27.3181(13)	16.6466(14)	30.8061(11)	10.8720(8)
θ (deg)		127.8392(16)	96.0445(16)	113.9130(13)	
V (Å^3)	7997.2(7)	8293.5(7)	9201.9(13)	9393.1(6)	4911.9(12)
Z	16	16	16	16	8
ρ (g•cm^{-3})	2.567	2.485	2.381	2.333	2.231
μ (mm^{-1})	16.851	16.250	14.653	27.845	13.726
θ range for data collection (deg)	3.2933 -33.1071	3.050-30.508	2.9379-32.9525	2.887-80.383	2.846-33.669
data/restraints/parameters	7627/0/262	12660/3/539	27578/994/1457	19475/1200/1461	12530/414/695
completeness (%)	99.8	99.7	98.2	94.7	88.5
GOF on F^2	1.142	1.123	1.034	1.077	0.956
R(int)	0.0445	0.0333	0.0454	0.0438	0.0470
R indices [I > 2σ(I)][a]	R_1 = 0.0314, wR_2 = 0.0621	R_1 = 0.0235, wR_2= 0.0528	R_1 = 0.0387, wR_2 = 0.0818	R_1 = 0.0271, wR_2 = 0.0624	R_1 = 0.0335, wR_2 = 0.0680
R indices (all data)[a]	R_1 = 0.0441, wR_2 = 0.0696	R_1 = 0.0275, wR_2= 0.0541	R_1 = 0.0627, wR_2 = 0.0929	R_1 = 0.0309, wR_2 = 0.0644	R_1 = 0.0623, wR_2 = 0.0746
Flack parameter					-0.019(6)
largest diff. peak and hole (e•Å^{-3})	3.54 and -2.33	3.16 and -1.35	2.42 and -1.64	0.976 and -1.169	1.17 and -1.46

[a] $R_1 = \Sigma||F_o| - |F_c||/\Sigma|F_o|$ $wR_2 = [\Sigma w(F_o^2-F_c^2)^2/\Sigma w(F_o^2)^2]^{1/2}$

In **2**, an interstitial water molecule was refined as partially occupied. Its O-H distances were restrained to 0.84(2) Å and the H···H distance to 1.36(2) Å. The occupancy rate refined to 0.311(13). In **3**, two of the biphenyl-2-carboxylate ligands and lead atom Pb8 are disordered with a common occupancy ratio. The disordered moieties were restrained to have similar geometries as another well defined ligand of the same kind. One of the phenyl rings (C73-C78) was constrained to resemble an ideal hexagon with C-C bond distances of 1.39 Å. U_{ij} components of ADPs for disordered atoms closer to each other than 2.0 Å were restrained to be similar. Subject to these conditions, the occupancy ratio refined as 0.722(4) to 0.278(4). The minor moieties of neighboring chains are in close contact with each other. The less than 50% occupancy for this ligand fragment does, however, avoid any necessary close contacts. In compound **5**, one of the biphenyl-3-carboxylate ligands was refined as disordered over two moieties. The two disordered moieties were restrained to have similar geometries. U_{ij} components of ADPs for disordered atoms closer to each other than 2.0 Å were restrained to be similar. Subject to these conditions, the occupancy ratio refined as 0.640(18) to 0.360(18).

Volume Calculations. Ligand noncoordinating to coordinating volume ratios were calculated using the method developed for previously reported lead oxide carboxylate ligands.[21] The atomic coordinates for each ligand were extracted from the crystallographically determined structures of **1**, **2**, **3**, and **5**, and spheres of appropriate van der Waals radius were placed at the atomic positions. Spheres corresponding to oxygen atoms were designated as coordinating, spheres corresponding to carbon and hydrogen atoms were designated as noncoordinating, and the total coordinating and noncoordinating volumes were calculated. The volumes shared by overlapping spheres were evenly divided between the component spheres to ensure that volume was not double-counted. To obtain the volume ratio, the noncoordinating volume was divided by the coordinating volume. This process was repeated using a set of coordinates obtained for each gas-phase ligand from geometries optimized using Gaussian 09 through the WebMO interface.[32,33] Calculations were run using the MP2 theory with the 6-311+G(2d,p) basis set.

Noncovalent Interaction (NCI) Index Calculations. NCI analyses were performed using CRITIC 2 version 1.0[34,35] to generate promolecular densities from the default numerical free-atom densities, using an approach similar to that described in a previous report.[36] The extraction of isosurfaces corresponding to particular interactions was performed using Mathematica[37] and visualized using Vesta.[38]

Results and discussion

Synthesis. Compounds **1**-**5** were successfully synthesized under solvothermal conditions. As with other lead oxide carboxylates containing aromatic ligands, larger product crystals grew in solvents containing small-chain alcohols than in water alone.[21]

Mixed solvents as well as very slow cooling rates were used to prepare large single crystals. Temperatures in the range of 150 °C to 220 °C were found to be the most effective in preparing the target compounds, with lower temperatures leading to incomplete reaction of lead oxide and higher temperatures resulting in reduction to form elemental lead.

For most of the compounds, reaction mixtures containing diffraction-quality single crystals were not phase-pure, and modified synthetic conditions were needed to obtain pure powders. PXRD identified plumbonacrite, a lead hydroxy-carbonate with the stoichiometry $Pb_5O(OH)_2(CO_3)_3$, as an impurity in initial syntheses.[39,40] Sonication and sparging of reaction mixtures to remove dissolved carbon dioxide prior to heating significantly increased the product purity, but small hexagonal crystals typical of plumbonacrite remained amidst the acicular crystals of the desired products. For syntheses of **1** and **3**, the plumbonacrite crystals were small relative to single crystals of the desired products and could be physically removed via suction filtration through a Hirsch funnel with appropriately sized pores and no filter paper. For **5**, a very slow cooling rate of 0.01 °C/min increased the size difference between phases to allow this separation, though at the expense of the yield of the desired phase. The high purity of **1, 3,** and **5** isolated via this method was confirmed by PXRD and elemental analysis.

Sonication and sparging not only minimized the plumbonacrite impurity in these syntheses but also played a critical role in polymorph selection between **3** and **4**. Reaction mixtures that were not sonicated and sparged prior to heating gave rise to **3**. Sonication and sparging of the initial reaction mixtures along with cooling at 0.1 °C/min gave rise to each polymorph in different trials of the same synthetic protocol. A combination of sonication, sparging, and slower cooling at 0.01 °C/min reproducibly resulted in selection of **4**. Sonication has previously been reported to influence polymorph selection of both inorganic and organic compounds, though mostly through application during crystallization.[41-43] In this case, a slurry of starting materials was sonicated prior to heating. Sonication of slurries is known to reduce particle sizes through sonofragmentation and interparticle collisions,[41] and this or a change in particle morphology may then affect polymorph selection through the kinetics of dissolution and nucleation during the reaction.

Despite much optimization, PXRD of a bulk sample of **2** (Figure S7, ESI) showed a minor phase impurity that is believed to be lead 2-naphthoate. Initial solvothermal synthesis of **2** resulted in formation of both acicular crystals of the desired product and a plate-like solid impurity. The abundance of plate-like crystals and the intensity of impurity peaks in PXRD patterns both increased when the molar ratio of PbO to 2-naphthoic acid in the reaction mixture was changed from 1:1 to 1:2. This suggests that the impurities are favored under conditions of high ligand concentration and/or low pH. Simple lead carboxylate phases that are favored under these conditions have been observed in syntheses of other lead oxide carboxylates,[44,45] and these lead carboxylates typically form two-dimensional structures, consistent with the plate-like crystals observed in the synthesis of **2**. To minimize the impurities, PbO and 2-naphthoic acid were heated with only a few drops of solvent -- a method that has previously minimized lead carboxylate contamination in synthesis of lead oxide carboxylates.[21,22] However, even with this optimization, residual diffraction peaks indicated that a minor impurity phase remained.

Thermal Analysis. As has been observed for other lead oxide carboxylates,[21] compounds **1**-**5** have high thermal stabilities for hybrid compounds and can be heated to nearly 400 °C before undergoing significant decomposition. The TGA traces of **1**-**5** are shown in Figures S11-15 in the ESI. While all the compounds were virtually colorless as synthesized, the powders recovered after TGA experiments had the red or yellow color of α- or β-lead oxide. With the exception of compound **2**, for which remaining impurities were discussed above, all compounds showed agreement within 1.0% between the observed mass loss and that predicted for decomposition to PbO. A sample of **1** showed a mass loss of 42.2% between 350 °C and 475 °C, in agreement with prediction. The observed loss for a sample rich in **2** was 45.0%, greater than the predicted loss of 42.4%. The discrepancy between predicted and observed mass losses reflects the presence of residual impurities in the sample.

Both compounds **3** and **4** showed steep mass losses around 400 °C with decreases in mass continuing up to around 500 °C. The predicted mass loss for **3** and **4** is 45.9%. The observed loss for **3** was 46.7% and the observed loss for **4** 46.1%. Compound **5** showed a mass loss occurring in two steps, one centered at approximately 415 °C, and the other centered at approximately 500 °C. The overall observed mass loss over the two steps was 46.5%, in comparison with a predicted loss of 45.9%.

Pb^{2+} Coordination Environments. The asymmetric unit for each structure is shown in the ESI (Figures S1-S5), as are the coordination environments for the crystallographically unique Pb^{2+} atoms (Figures S16-S20). Pb^{2+} atoms in all five of the structures are coordinated both by oxide anions and by oxygen atoms of the carboxylate ligands. The oxide coordination takes place at relatively short distances of 2.20-2.35 Å, while the carboxylate oxygens coordinate at greater distances. In analysis of the coordination numbers and geometries, the maximum Pb-O lengths to be considered as bonds were determined through calculation of bond valence sums[46,47] (Table S1, ESI) and looking for gaps in the distribution of Pb-O contact distances. The two crystallographically unique Pb^{2+} centers in **1** are in irregular 7-coordinate geometries while the four unique metal centers in **2** are in irregular 6- and 7-coordinate geometries. Structures **3** and **4** each have eight crystallographically unique lead atoms with coordination numbers of 6-8, whereas the four Pb^{2+} centers in **5** are 6- or 7-coordinate, again with irregular geometries. The coordination geometries in all the structures are hemidirected, with oxygen atoms located primarily in half of each coordination sphere.[48] These asymmetric coordination geometries are qualitatively similar to those in lead oxide carboxylates with substituted benzoate ligands, for which calculation of electron localization functions previously showed that the gaps in the coordination spheres were occupied by electron density associated with $6s^2$ lone pairs.[21]

Helical One-Dimensional Lead Oxide Substructures. All five novel lead oxide carboxylates have the stoichiometry Pb_2OL_2 where L is the carboxylate ligand. The inorganic substructures occur as extended, one-dimensional, helical Pb_2O^{2+} chains composed of distorted, edge-sharing Pb_4O tetrahedra. Carboxylate oxygen atoms further coordinate the lead atoms in the inorganic chains, with the noncoordinating volume of the ligands extending into the space between the inorganic cores. These helical substructures have previously been observed in lead oxide carboxylates with benzoate-based ligands. [21,22] As discussed above, local asymmetries occur in the coordination sphere around each hemidirected lead atom, but we do not believe these to be the cause of the non-centrosymmetry of the extended chains. As a counterexample, linear, non-helical Pb_2O^{2+} chains were previously observed in $Pb_2O(CHOO)_2$, even though that compound also contains hemidirected lead coordination sites.[19] This indicates that neither the Pb_2O^{2+} stoichiometry nor the locally asymmetric lead sites necessarily leads to formation of helices. Rather, the distortion of the Pb_4O tetrahedra and the resulting helical chains may occur in some compounds to optimize ligand packing between chains, with the benefits of efficient space filling and increased van der Waals contacts between ligands. We have undertaken analysis of noncovalent interactions (*vide infra*) in part to determine the nature of these weak interchain interactions.

Symmetries and Packing of One-Dimensional Hybrid Motifs. In a previous study of lead oxide carboxylates, the overall dimensionality of the structures was correlated with the ratio of noncoordinating to coordinating volume in the ligands. Among the previously characterized compounds, ligands with ratios in the range of 4-5 formed one-dimensional compounds, with lower values leading to higher dimensionalities.[21] All four of the ligands in our current group have ligand volume ratios of over 6 (Table 2). The new structures show no bridging of chains by organic ligands, leading to one-dimensional structures in keeping with the established trend.

Although the helical inorganic substructures in **1**-**5** show the same connectivities and general geometries, the one-dimensional hybrid motifs are packed differently in the structures, and the overall space groups and symmetries change with ligand identity. Compound **1**, shown in Figure 2, crystallizes in the tetragonal space group $I4_1/a$. Hybrid chains extend in the z direction and are patterned in a square net in the xy plane.

Table 2. Calculated ligand volume ratios for ligands in **1**-**5**.

ligand	ratio based on crystal structures	ratio based on *ab initio* calculations
1-naphthoate	6.2	6.4
2-naphthoate	6.2	6.5
biphenyl-2-carboxylate	7.4	7.4
biphenyl-3-carboxylate	7.4	7.5

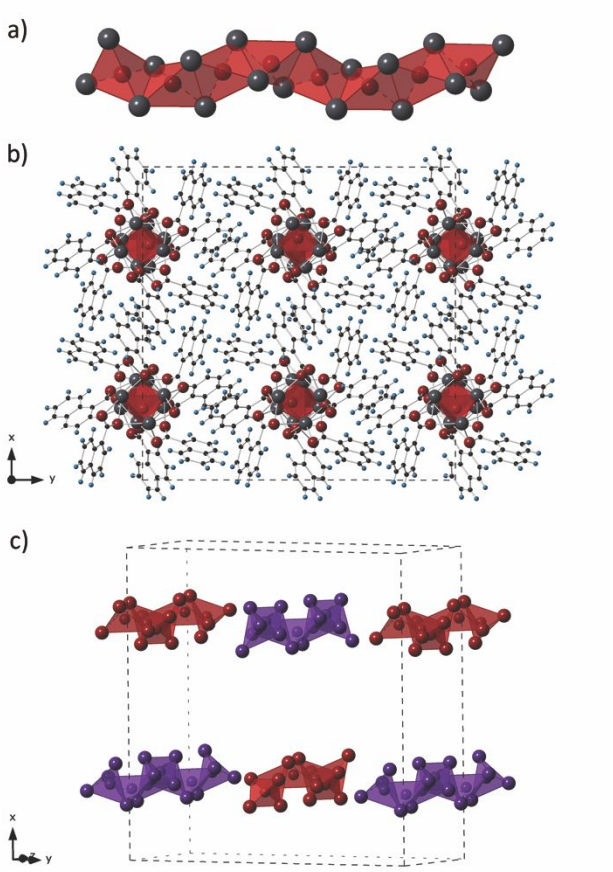

Figure 2. a) Helical Pb_2O^{2+} chain in **1**. b) Unit cell for **1**. c) Right-handed (red) and left-handed (purple) helices in **1**. Lead atoms are shown in gray, oxygen atoms in red, carbon atoms in black, and hydrogen atoms in blue.

The chiral chains are coincident with 4-fold screw axes, but adjacent helices are related by inversion, resulting in a globally centrosymmetric crystal structure. Nearest neighbors of the same chirality are related by two-fold rotation. The patterning of left and right handed helices is shown in Figure 2c.

Shown in Figure 3, **2** crystallizes in the monoclinic space group $C2/c$. Hybrid chains are extended in the y direction and patterned in an oblique net in the xz plane. The inorganic cores contain nominal 4-fold screw axes, but the four tetrahedra in the repeat unit of each helix occur as two crystallographically distinct pairs, breaking the symmetry. The chiral hybrid chains are coincident with true 2-fold screw axes. Helices in rows parallel to the x-axis are related to the helices in adjacent rows by inversion, resulting in a globally centrosymmetric crystal structure. Along the x-direction, adjacent helices of the same chirality are related by two-fold rotation. The patterning of left and right handed helices is shown in Figure 3b.

Shown in Figure 4, compound **3** crystallizes in the monoclinic space group $P2_1/c$. Hybrid chains are extended in the x direction and are patterned in an approximately hexagonal net in the yz plane. The inorganic cores are coincident with *pseudo*-4-fold screw axes, but the four tetrahedra in the repeat unit are all crystallographically distinct, breaking the 4-fold screw symmetry. However, in a given row of helices parallel to the y-axis, hybrid chains are related to each other by a 2-fold screw

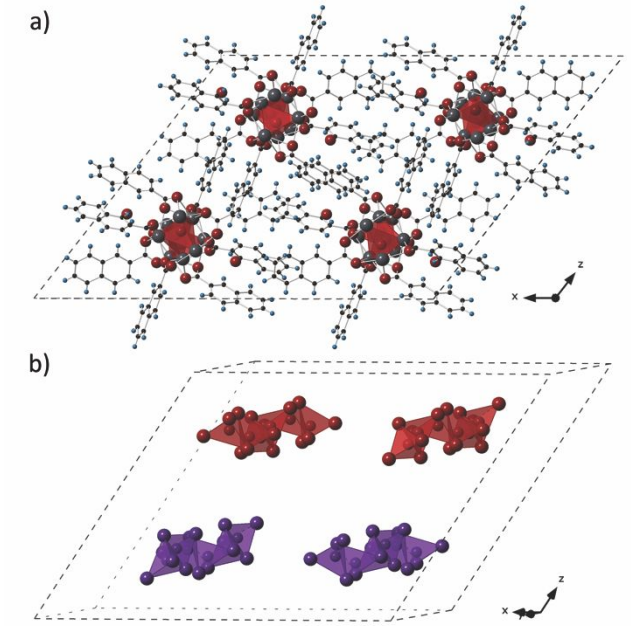

Figure 3. a) Unit cell for **2**. b) Right-handed (red) and left-handed (purple) helices in **2**. Lead atoms are shown in gray, oxygen atoms in red, carbon atoms in black, and hydrogen atoms in blue.

axis that skewers them along the y direction, such that a hybrid chain is regenerated upon rotating 180° in the xz plane and translating half a unit cell in the y direction. Each of these rows of hybrid chains is related to the adjacent rows by inversion, resulting in a globally centrosymmetric crystal structure. This causes each hybrid chain to have four neighbors with the opposite chirality to its own. However, adjacent chains in the z direction are related by translation and are all of the same chirality. The patterning of the left and right handed helices coincident with the hybrid chains is shown in Figure 4b. Because the hybrid chains do not have true screw symmetry, the asymmetric unit runs the full length of the cell in the x-direction and consists of four crystallographically distinct Pb_2OL_2 formula units.

Compound **4** (Figure 4c) crystallizes in the monoclinic space group $P2_1/c$. Hybrid chains are extended in the y direction, and they are patterned in an oblique net in the xz plane. The *pseudo*-4-fold symmetry of the inorganic core is broken as the four tetrahedra in the repeat unit occur as two crystallographically distinct pairs. The hybrid chains are coincident with true 2-fold screw axes. There are two crystallographically distinct hybrid chains that alternate in the x direction. Chains are related to those of opposite chirality through inversion centers, resulting in a globally centrosymmetric crystal structure. The patterning of left and right handed helices is shown in Figure 4d.

Compound **5** (Figure 5) crystallizes in the tetragonal space group $P4_1$. Hybrid chains in **5** are extended in the z direction and are patterned in a centered square net in the xy plane. The structure contains two crystallographically independent chains, both of which form right-handed helices. Thus, though both of the helices in the unit cell have the same chirality, they are related only by *pseudo*-translation. The hybrid chains are coincident with 4-fold screw axes, and helices are not related to each other by inversion, nor are they perpendicular to a 2-fold

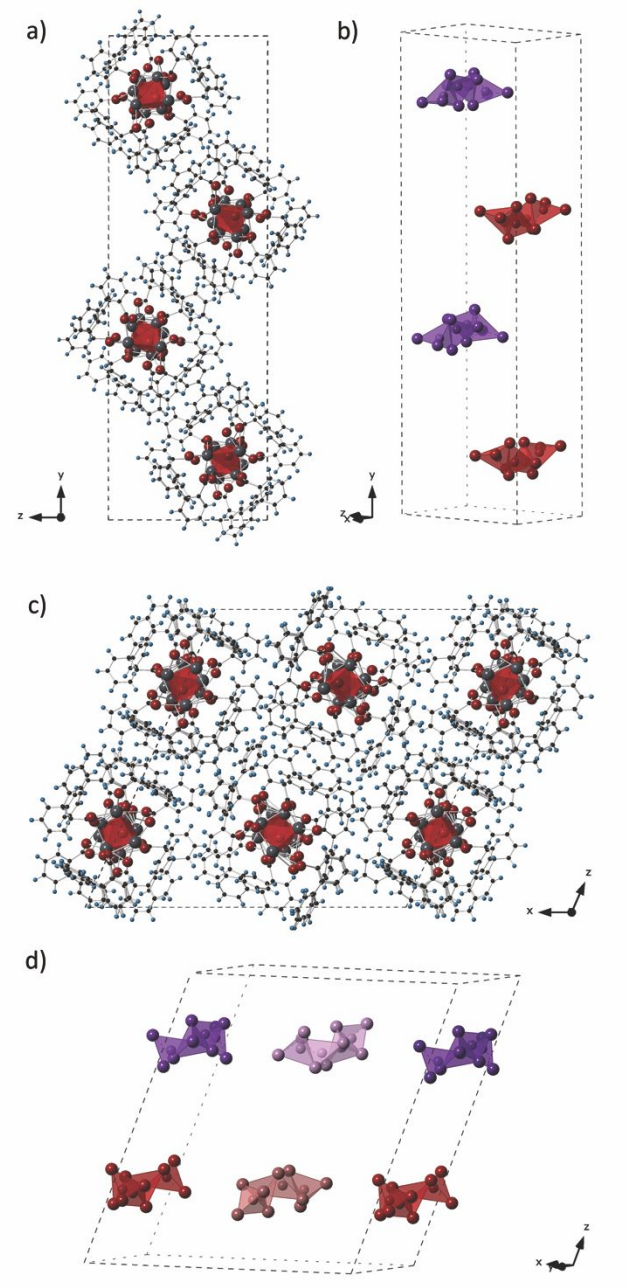

Figure 4. a) Unit cell for **3**. b) Right-handed (red) and left-handed (purple) helices in **3**. c) Unit cell for **4**. d) Crystallographically unique right-handed helices (red and pink) and crystallographically unique left-handed helices (purple and light purple) in **4**. Lead atoms are shown in gray, oxygen atoms in red, carbon atoms in black, and hydrogen atoms in blue.

axis or mirror plane. This results in a polar, chiral crystal structure. The crystallographic finding of non-centrosymmetry was corroborated by detection of second-harmonic generation. The intensity of light at the second harmonic frequency was found to be comparable to that of the standard α- SiO_2.

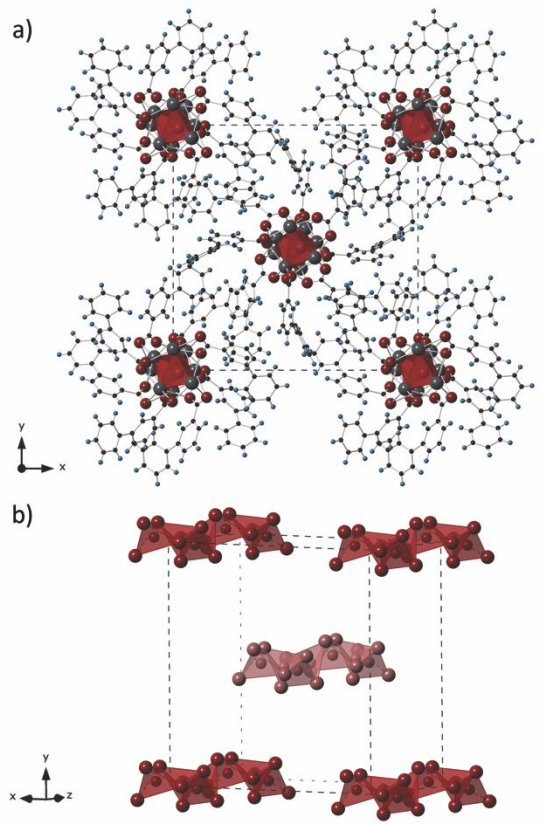

Figure 5. a) Unit cell for **5**. b) Crystallographically unique right-handed helices (red and pink) in **5**. Lead atoms are shown in gray, oxygen atoms in red, carbon atoms in black, and hydrogen atoms in blue.

Influences of Ligand Shape on Packing of One-Dimensional Motifs. The one-dimensional hybrid motifs in **1**-**5** are nominally cylindrical. Hard cylinders of uniform diameter would ideally be expected to pack in a hexagonal array. The structures here form a variety of nets, only one of which is approximately hexagonal. Among the factors differentiating these structures from hard cylinders are the shapes of the ligands, the way they fill space, and the extent to which they allow for interdigitation among ligands from neighboring chains. These factors can be connected with the pattern of packing observed in each structure.

In **1** and **2**, the carboxylate groups of the naphthoate ligands coordinate Pb_2O^{+2} chains, and the noncoordinating volume of the ligands extends into the space between chains. In **1**, the angle between the ring-carboxylate bond and the centroid-centroid axis is 90° (Figure 1), and the bulk of the ligand volume is aligned approximately parallel to the length of the inorganic motif. As shown in Figure 6a, this provides effective space filling around a given inorganic chain by the noncoordinating volume of the ligands. On the other hand, in **2**, the larger angle between the ring-carboxylate bond and the centroid-centroid axis causes the noncoordinating volume of the 2-naphthoate ligands to extend away from the inorganic motifs (Figure 6b). The noncoordinating volumes of the 1-naphthoate and 2-naphthoate ligands are approximately equivalent, but because 2-naphthoate extends further from the inorganic chains than does 1-naphthoate, it does not fill space around the chains as effectively as ligands in **1**, leaving more accessible space near the inorganic core.

Ligands in **1** wrap around their associated extended inorganic motifs in a densely packed helical pattern. As can be seen in the end-on view in Figure 6c, the noncoordinating volume of the ligands occupies the space directly surrounding the inorganic motif, save for a small opening that occurs once per quarter turn of the helix. Ligands anchored on adjacent chains cannot penetrate the steric bulk of the densely packed helices, and so they penetrate close to the inorganic chain of interest only via these small openings that occur with 4-fold screw symmetry around the chain. Because of this, a given hybrid chain is bordered by neighboring hybrid chains on four sides, corresponding to the square mesh patterning of chains within the unit cell.

Because ligands in **2** extend away from their associated inorganic motifs, they occupy the space immediately surrounding the inorganic chain less effectively than in **1**. As shown in Figure 6b, ligands from neighboring chains interdigidate, penetrating into the open spaces left by ligands coordinating the inorganic core. Rather than radiating uniformly from this core, the ligands in **2** bend toward one another, perhaps in order to optimize their packing. One of the

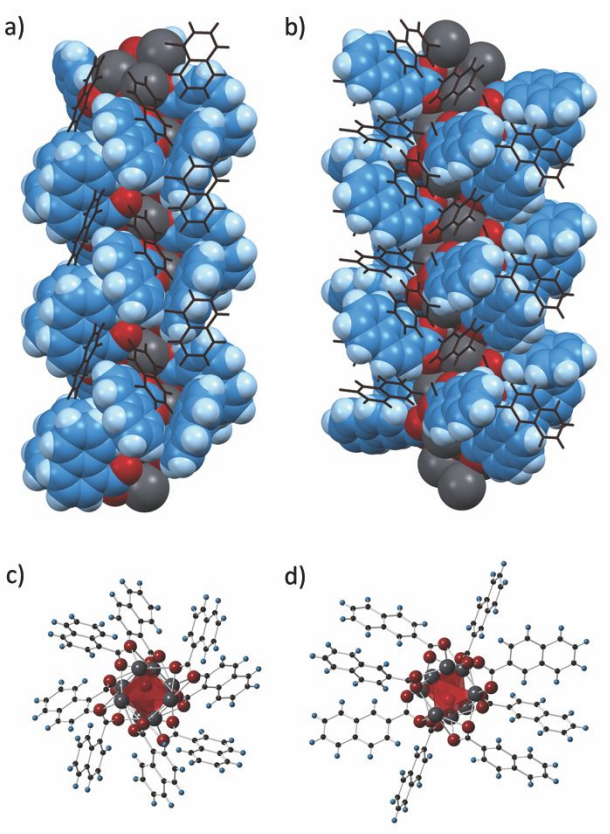

Figure 6. a) Space-filling diagram of one chain in **1** with ligands from a neighboring chain shown as sticks, indicating little interdigitation in the space nearest the inorganic core. b) Space-filling diagram of one chain in **2** with ligands from neighboring chains shown as sticks, indicating greater interdigitation of ligands on the chains. End-on views of the chains in **1** and **2** are shown in c) and d), respectively.

ligands on **2**, in particular, is dramatically bent toward other ligands on the same chain (Figure 6d), opening up a large pocket around the inorganic motif, in which organics from multiple adjacent chains pack together. The chains in **2** have two-fold screw symmetry, and the monoclinic unit cell and oblique mesh patterning of chains in **2** allow six neighboring chains to interpenetrate with any given one, such that ligands from multiple neighboring chains come together and interdigitate in the large pockets. The crystallographically determined density of **2** is lower than that of **1**, consistent with less effective space-filling. Its crystallization as a hydrate may also be because vacant sites occur for water to occupy in the structure.

Compared with the naphthoate ligands, biphenyl-2-carboxylate and biphenyl-3-carboxylate have greater flexibility due to the torsional variability between their aromatic rings. Both space-filling and end-on views (Figure 7) show that in **3**, this flexibility allows the ligand to fill space very effectively by wrapping around the inorganic chain, leaving virtually no unfilled space near the inorganic motif. Ligands on adjacent chains do not interdigitate, and the chains form a closest packed mesh geometry. Among the five structures reported here, this is the only one that packs in approximately the hexagonal pattern that would be expected for hard cylinders, in keeping with the limited interdigitation between chains. In **4**, which is a polymorph of **3**, there are two crystallographically independent chains. While the angling of the ligands opens up slightly larger pockets of space around the inorganic chains than in **3**, interdigitation does not occur. This may be seen in Figure 8a, where ligands from neighboring chains do not occupy the spaces available near the inorganic cores of a central chain.

In **5**, which also has two crystallographically independent chains, biphenyl-3-carboxylate extends further from the inorganic core than biphenyl-2-carboxylate due to the greater-than-90° angle formed between the ring-carboxylate bond and the main volume of the ligand. This distribution of volume means that more open space exists near the inorganic cores. As in **2**, there is significant interdigitation between ligands on adjacent chains. As Figure 8b illustrates, ligands from neighboring chains penetrate into the unoccupied volume near an inorganic core. The end-on view in Figure 8d shows that the ligands in **5** leave pockets occurring with 4-fold screw symmetry along the length of the chain, corresponding to the packing of chains in a net in which each has four nearest neighbors. The crystallographically determined density of **5** is less than that of **3** and **4**, further illustrating the less efficient filling of space by the more projecting ligand.

From the comparisons between **1** and **2** and among **3**, **4**, and **5**, we can conclude that the orientation of a ligand's noncoordinating volume, in addition to the ligand volume ratio, is an important influence in formation of these hybrid structures. The efficiency of the space-filling immediately around the inorganic core is dependent on the ligand shape. Structures in which the space-filling is more efficient pack in nearly hexagonal patterns that approach the ideal closest-packing of hard cylinders. Less efficient space-filling allows interdigitation of ligands from neighboring hybrid chains, and the positions of pockets for interdigitation correspond to the observed packing symmetries.

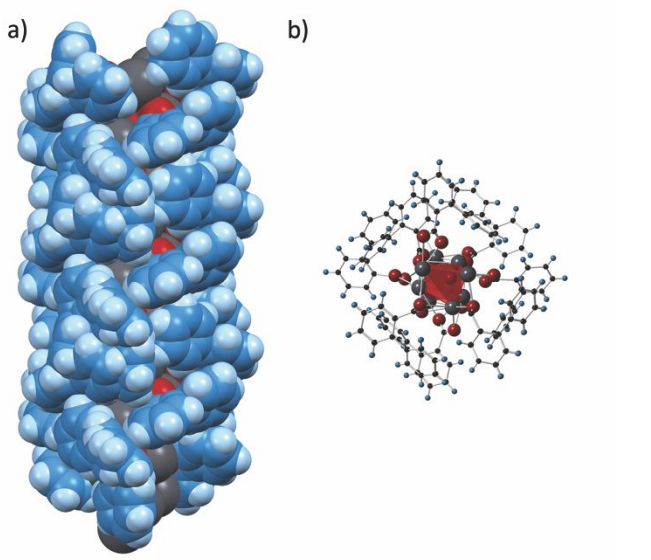

Figure 7. Space-filling (a) and end-on (b) representations of chain in **3** showing effective filling of space immediately around the inorganic core.

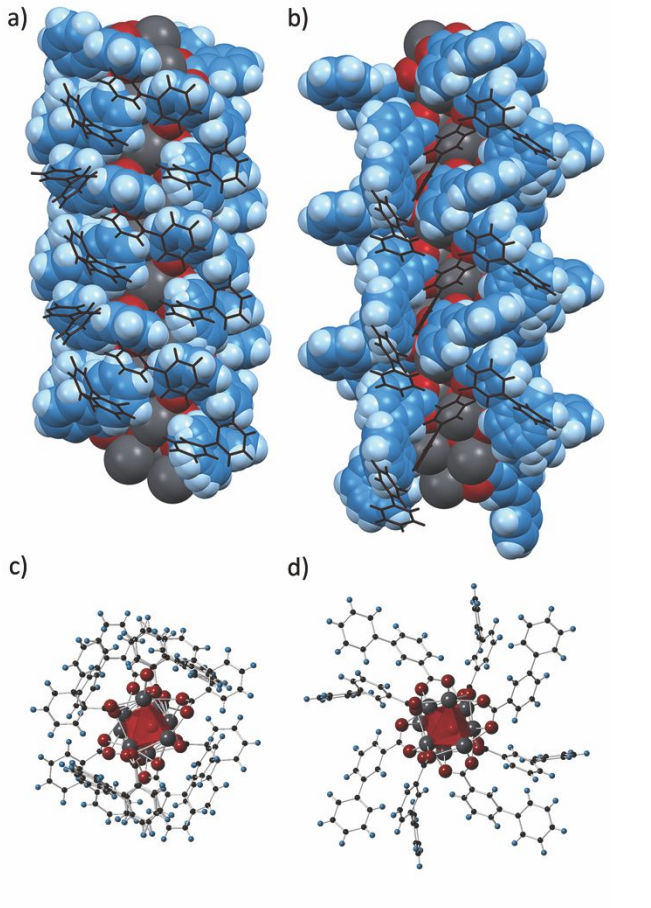

Figure 8. Space-filling representations of chains in **4** (a) and **5** (b) with ligands from neighboring chains shown in stick form. End-on views of the chains are shown in c) and d), respectively.

Visualization of Electron Densities Associated with Noncovalent Interactions in 1 and 2

NCI index calculations were carried out for **1** and **2** in order to quantify and visualize areas of electron density associated with noncovalent interactions in the structures. Because input files for the NCI method cannot include disorder or partial occupancy, the solvent water occupancy in **2** was set to 1 for the calculations. Due to the more extensive disorder in the structures involving the biphenylcarboxylates, this analysis was not undertaken for **3**-**5**. The NCI method generates plots of the reduced density gradient, s, versus sign(λ_2)ρ that serve as NCI fingerprints for the structures. Spikes in the fingerprints are associated with noncovalent interactions, with attractive interactions occurring at negative sign(λ_2)ρ and stronger interactions corresponding to higher absolute values of sign(λ_2)ρ. Visualization of electron density isosurfaces for interactions between -0.08 and 0.05 sign(λ_2)ρ showed the location and type of interaction associated with each spike. Plots of the reduced density gradients versus the electron densities for attractive interactions in **1** and **2** are shown in Figure 9 and those for repulsive interactions in Figure 10. For both **1** and **2**, the strongest noncovalent attractions -- indicated by spikes at larger, negative values of sign(λ_2)ρ -- come from ionic interactions within the inorganic substructures. Ionic interactions also contribute weakly to the repulsive interactions in the structures. Visualization of these interactions shows the interplay of attraction between Pb^{2+} and O^{2-} ions and the repulsions among Pb^{2+} ions in stabilizing the inorganic chains (Figure 11). Pb-O contacts involving carboxylate oxygen atoms are weaker than those with oxide anions, though both are significant in stabilizing the structures. Comparison of the plots for **1** and **2** shows a clustering in the attractive interactions for **1** that is not observed for **2**. This is consistent with the Pb-O bond lengths. For **1**, there are no Pb-O contacts between 2.45 Å and 2.73 Å, providing a gap in lengths that corresponds to the gap in interaction strengths. For **2**, there are many more unique Pb-O contacts due to the lower symmetry of the structure, and the distribution

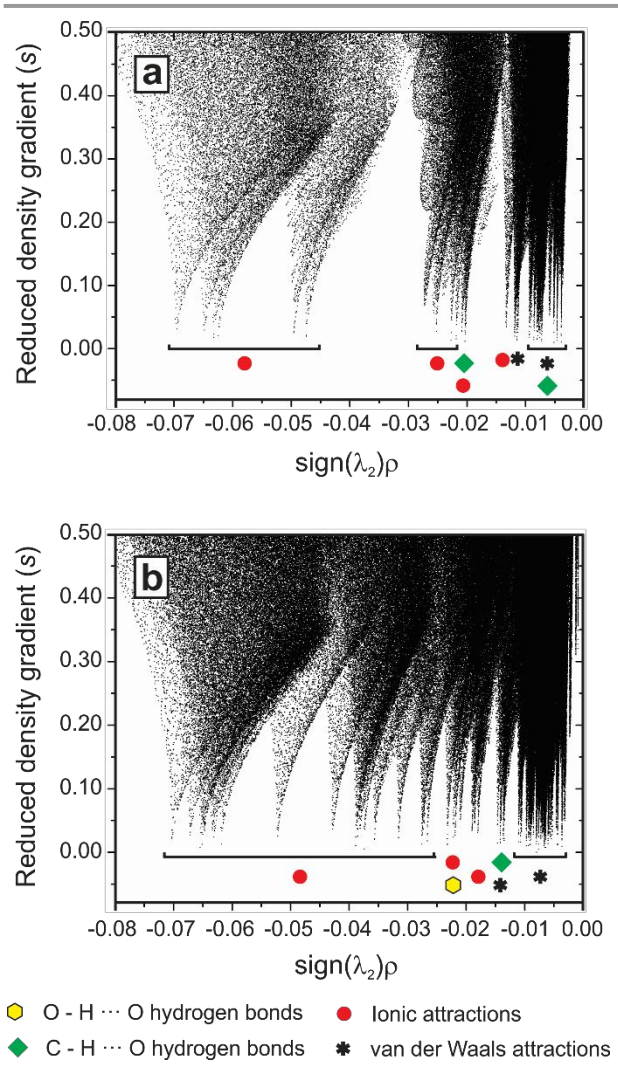

Figure 9. NCI analysis of **1** (a) and **2** (b) showing attractive interactions.

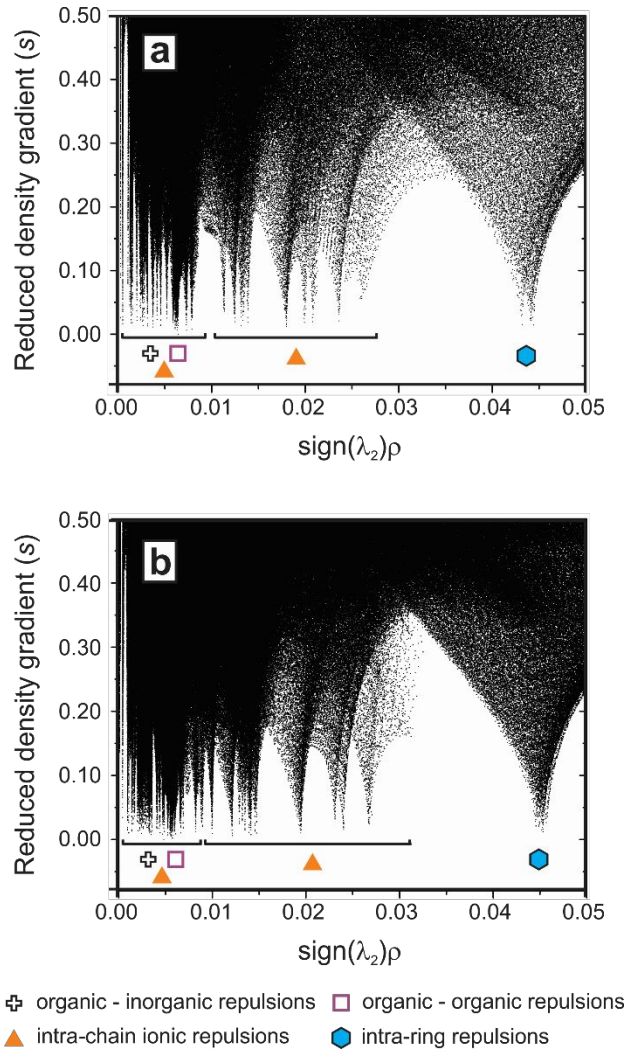

Figure 10. NCI analysis of **1** (a) and **2** (b) showing repulsive interactions.

of Pb-O bond lengths contains no gap of more than 0.1 Å between 2.25 Å and 2.97 Å. NCI analyses for **1** and **2** also corroborate our bond valence sum analyses. The longest Pb-O contacts included in the sums were 3.19 Å and 3.14 Å, respectively, for **1** and **2**, even though for **2**, this distance was greater than 0.1 Å longer than the next-longest contact that was considered. The NCI visualization confirmed electron density consistent with ionic bonding for these long interactions.

Weaker attractions classified as van der Waals attractions in both **1** and **2** include interactions among the aromatic naphthoate ligands. As has previously been reported in studies of organic crystals as well as metal complexes with organic ligands, the observed interactions are either edge-face, in which one aromatic ring is nominally perpendicular to the other, or offset face-face, in which rings are approximately parallel but displaced.[49-52] Eclipsed face-face interactions were not observed. The aromatic-aromatic packing motifs observed in **1** and **2** are different from those in the crystal structures of the corresponding ligand acids.[53] One important underlying difference is that the acid structures are strongly influenced by the formation of carboxylic acid dimers that are not present in the hybrids, but we also observe that the packing patterns among ligands in the hybrid materials are influenced by their coordination to the inorganic cores.

The strongest aromatic-aromatic interactions in both compounds are edge-face. Such geometries are understood to result from weak hydrogen-bonding interactions between hydrogen atoms on one ligand and delocalized π clouds on another.[50] The strongest edge-face interaction in **1** is shown in Figure 12a. The centroid-centroid distance associated with this interaction is 4.87 Å, while the distance from the centroid of one ring to the nearest hydrogen atom of the approximately perpendicular ring is 2.58 Å. The centroid-C—H angle is 163.8°. In comparison with a survey of C—H-π interactions in organic crystals, the interaction in the present structure is slightly shorter but more linear than the mean, in keeping with the observed trend of greater linearity with increasing strength.[49] Pairs of ligands coordinated to different inorganic chains interact with one another in this way, and their symmetry equivalents lead to tetrameric pinwheels of ligands (Figure 12b).

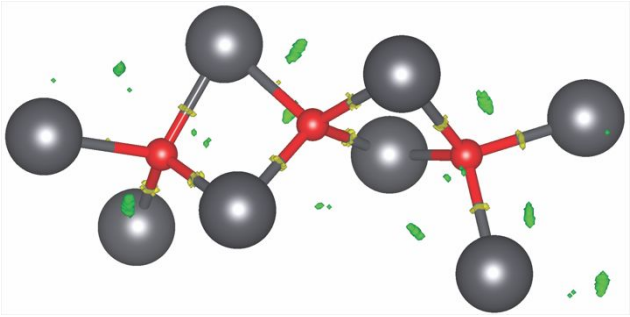

Figure 11. Fragment of Pb_2O^{2+} chain in **1** showing electron densities associated with Pb-O ionic attractions (yellow) and Pb-Pb repulsions (green).

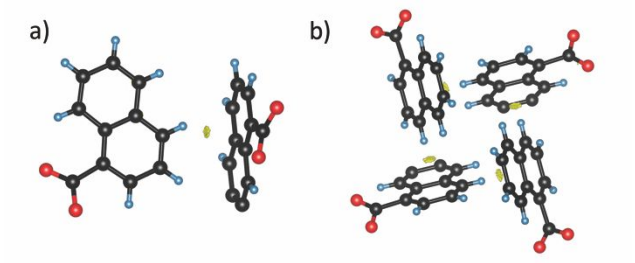

Figure 12. Areas of electron density associated with edge-face aromatic-aromatic interactions in **1**.

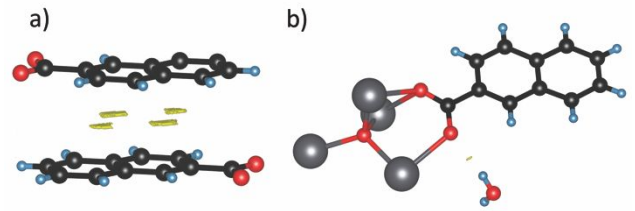

Figure 13. Areas of electron density associated with offset face-face (a) and hydrogen bonding (b) interactions in **2**.

The organic-organic interactions in **2** are more varied than in **1**, in keeping with the lower symmetry of the structure. While this structure does include edge-face interactions, it also contains offset face-face interactions that are stronger than any interaction of this type in **1**. Figure 13a shows the strongest such offset face-face interaction, in which the entire aromatic system of a ligand on one inorganic chain interacts with the corresponding ligand on another chain. This interaction is consistent with the interdigitation observed in **2** due to the greater directionality of the ligands away from the inorganic chains in comparison with **1**. The centroid-centroid distance of 3.74 Å observed here is in agreement with the mode observed for the nearest interactions in metal complexes with quinolone-based ligands.[52] Structure **2** also contains multiple areas where ligands from three different neighboring chains all interact with each other around the surface of the inorganic motifs, which is not observed in **1** and is consistent with the greater degree of interdigitation observed in **2**.

Structure **2** also contains hydrogen-bonding interactions involving the water molecule of hydration. The strongest of these is an OH—O interaction with a carboxylate oxygen atom (Figure 13b). The donor-acceptor distance of 2.947 Å is indicative of a moderately strong, primarily electrostatic interaction.[54] The electron density maps for both **1** and **2** also indicate weaker CH—O hydrogen bonding interactions in both structures.

Conclusions

Despite their organic ligands having similar noncoordinating to coordinating volume ratios, the five novel lead oxide carboxylates presented here all have unique space group symmetries as well as differences in density and thermal stability. Helical inorganic motifs exist in each structure, yet just one has a globally chiral crystal structure and accompanying

nonlinear optical activity. Thus, it is apparent that subtle changes in ligand shape, such as different ring positions of coordinating substituents, can cause hybrid materials to have different global symmetries and properties. It had been shown previously that changes in ligand volume ratio cause changes in structural dimensionality. Here we have shown that changing the ligand shape via the orientation of the noncoordinating volume with respect to the coordinating carboxylate group causes changes in crystal structure and symmetry. This finding complements recent reports regarding the role of ligand shape in MOFs.[55-57] While these reports focused on differences in angles among coordinating groups on multitopic ligands, we have demonstrated the importance of the angle between the coordinating group in a monotopic ligand and the bulk of its noncoordinating volume.

With this set of novel lead oxide carboxylates, we make headway in demonstrating the principles governing the packing arrangements of extended inorganic hybrids, in which one must consider both space filling as well as spatial considerations imparted by the inorganic motif, such as fixation of the organics on inorganic chains. Ligands with shapes that provide very efficient space filling allow inorganic motifs to pack in arrangements nearly consistent with closest packing of ideal geometric objects such as cylinders. Less efficient space filling allows interdigitation of ligands from adjacent chains, and the packing geometries and symmetries of hybrid substructures are related to the size and position of the interdigitation sites. We have also found for the structures formed with 1- and 2-naphthoate that both edge-face and face-face interactions occur between aromatic rings, with face-face interactions more significant in the structure with greater interdigitation of ligands. The structural patterns found here may prove applicable to other hybrid systems containing one-dimensional, extended inorganic substructures.

Conflicts of interest

There are no conflicts to declare.

Acknowledgements

This material is based primarily on work supported by the National Science Foundation under Grant Number DMR-1151498. Additional support came from Oberlin College. Single-crystal XRD was performed on a diffractometer purchased through a National Science Foundation MRI grant (CHE-1625433). We acknowledge Professor P. Shiv Halasyamani (University of Houston) for assistance with the SHG measurement and Professor Alexander Norquist (Haverford College) for help and useful discussions about the NCI index calculations. The work of X.J. was supported by the National Science Foundation under Grant Number DMR-1709351. The work of W.Z. was supported by the Welch Foundation (Grant E-1457). This material is based upon work supported by (while serving at) the National Science Foundation. Any opinions, findings, and conclusions or recommendations expressed in this material are those of the authors and do not necessarily reflect the views of the National Science Foundation.

References

1 A. K. Cheetham, C. N. R. Rao and R. K. Feller, *Chem. Commun.*, 2006, 4780-4795.
2 R. Roccanova, W. Min, V. R. Whiteside, M. A. McGuire, I. R. Sellers, M.-H. Du and B. Saparov, *Inorg. Chem.*, 2017, **56**, 13878-13888.
3 B. Saparov and D. B. Mitzi, *Chem. Rev.*, 2016, **116**, 4558-4596.
4 J. T. Greenfield, C. Pak, S. Kamali, K. Lee and K. Kovnir, *Chem. Commun.*, 2015, **51**, 5355-5358.
5 R. K. Feller and A. K. Cheetham, *Solid State Sci.*, 2006, **8**, 1121-1125.
6 D. T. Tran, N. A. Chernova, D. Chu, A. G. Oliver and S. R. J. Oliver, *Cryst. Growth Des.*, 2010, **10**, 874-879.
7 B. Ahmed, H. Jo, S.-J. Oh and K. M. Ok, *Inorg. Chem.*, 2018, **57**, 6702-6709.
8 R. Gautier, K. Oka, T. Kihara, N. Kumar, A. Sundaresan, M. Tokunaga, M. Azuma and K. R. Poeppelmeier, *J. Am. Chem. Soc.*, 2013, **135**, 19268-19274.
9 S. Bouketaya, M. Smida, M. S. M. Abdelbaky, M. Dammak and S. García-Granda, *J. Solid State Chem.*, 2018, **262**, 343-350.
10 H. A. Evans, D. H. Fabini, J. L. Andrews, M. Koerner, M. B. Preefer, G. Wu, F. Wudl, A. K. Cheetham and R. Seshadri, *Inorg. Chem.*, 2018, **57**, 10375-10382.
11 H. H.-M. Yeung, W. Li, P. J. Saines, T. K. J. Köster, C. P. Grey and A. K. Cheetham, *Angew. Chem. Int. Ed.*, 2013, **52**, 5544-5547.
12 L. Luo, Y. Chen and P. A. Maggard, *J. Solid State Chem.*, 2020, **287**, DOI: 10.1016/j.jssc.2020121358.
13 A. G. Guillen, M. Oszajca, K. Luberda-Durnas, M. Gryl, S. Bartkiewicz, A. Miniewicz and W. Lasocha, *Cryst. Growth Des.*, 2018, **18**, 5029-5037.
14 J. C. Tan and A. K. Cheetham, *Chem. Soc. Rev.*, 2011, **40**, 1059-1080.
15 P. J. Saines, J.-C. Tan, H. H.-M. Yeung, P. T. Barton and A. K. Cheetham, *Dalton Trans.*, 2012, **41**, 8585-8593.
16 Y. Fu, X. Jiang, X. Li, B. Traore, I. Spanopoulos, C. Katan, J. Even, M. Kanatzidis and E. Harel, *J. Am. Chem. Soc.*, 2020, **142**, 4008-4021.
17 G. Kieslich, S. Sun and A. K. Cheetham, *Chem. Sci.*, 2014, **5**, 4712-4715.
18 W. Travis, E. N. K. Glover, H. Bronstein, D. O. Scanlon and R. G. Palgrave, *Chem. Sci.*, 2016, **7**, 4548-4556.
19 C. M. Mauck, T. W. P. van den Heuvel, M. M. Hull, M. Zeller and C. M. Oertel, *Inorg. Chem.*, 2010, **49**, 10736-10743.
20 F. Bonhomme, T. M. Alam, A. J. Celestian, D. R. Tallant, T. J. Boyle, B. R. Cherry, R. G. Tissot, M. A. Rodriguez, J. B. Parise and M. Nyman, *Inorg. Chem.*, 2005, **44**, 7394-7402.
21 E. E. Liu, C. Gang, M. Zeller, D. H. Fabini and C. M. Oertel, *Cryst. Growth Des.*, 2017, **17**, 1574-1582.
22 C. C. Easterday, L. R. Dedon, M. Zeller and C. M. Oertel, *Cryst. Growth Des.*, 2014, **14**, 2048-2055.
23 X.-S. Wu, Y.-X. Wang, S.-Q. Li, Y. Qian, L. Zhai, X.-Z. Wang and X.-M. Ren, Dalton Trans., 2018, **47**, 14636-14643.
24 H. Naïli, M. François, A. J. Norquist and W. Rekik, *Solid State Sci.*, 2017, **74**, 44-55.
25 X. Jia, J. L. Dixon, M. Zeller, J. Schrier and A. J. Norquist, *J. Solid State Chem.*, 2019, **273**, 158-165.
26 J. Munárriz, F. A. Rabuffetti and J. Contreras-García, *Cryst. Growth Des.*, 2018, **18**, 6901-6910.
27 K. M. Ok, E. O. Chi and P. S. Halasyamani, *Chem. Soc. Rev.*, 2006, **35**, 710-717.
28 Apex3 (V2016.9-0), Bruker AXS Inc., Madison, WI, 2016.
29 SAINT (V8.37A), Bruker AXS Inc., Madison, WI, 2016.

30 L. Krause, R. Herbst-Irmer, G. M. Sheldrick, D. Stalke, *J. Appl. Crystallogr.*, 2015, **48**, 3-10.
31 G. M. Sheldrick, *Acta Cryst.*, 2015, **C71**, 3-8.
32 M. J. Frisch, G. W. Trucks, H. B. Schlegel, G. E. Scuseria, M. A. Robb, J. R. Cheeseman, G. Scalmani, V. Barone, B. Mennucci, G. A. Petersson, H. Nakatsuji, M. Caricato, X. Li, H. P. Hratchian, A. F. Izmaylov, J. Bloino, G. Zheng, J. L. Sonnenberg, M. Hada, M. Ehara, K. Toyota, R. Fukuda, J. Hasegawa, M. Ishida, T. Nakajima, Y. Honda, O. Kitao, H. Nakai, T. Vreven, J. A. Montgomery Jr, J. E. Peralta, F. Ogliaro, M. J. Bearpark, J. Heyd, E. N. Brothers, K. N. Kudin, V. N. Staroverov, R. Kobayashi, J. Normand, K. Raghavachari, A. P. Rendell, J. C. Burant, S. S. Iyengar, J. Tomasi, M. Cossi, N. Rega, N. J. Millam, M. Klene, J. E. Knox, J. B. Cross, V. Bakken, C. Adamo, J. Jaramillo, R. Gomperts, R. E. Stratmann, O. Yazyev, A. J. Austin, R. Cammi, C. Pomelli, J. W. Ochterski, R. L. Martin, K. Morokuma, V. G. Zakrzewski, G. A. Voth, P. Salvador, J. J. Dannenberg, S. Dapprich, A. D. Daniels, Ö. Farkas, J. B. Foresman, J. V. Ortiz, J. Cioslowski and D. J. Fox, Gaussian 09 (Revision D.01), Gaussian, Inc., Wallingford, CT, 2009.
33 J. R. Schmidt and W. F. Polik, WebMO Enterprise (version 15.0.003e), WebMO LLC, Holland, MI, 2015.
34 A. Otero-de-la-Roza, M. A. Blanco, A. M. Pendás and V. C. Luaña, *Comput. Phys. Commun.*, 2009, **180**, 157-166.
35 A. Otero-de-la-Roza, E. R. Johnson and V. Luaña, *Comput. Phys. Commun.*, 2014, **185**, 1007-1018.
36 A. Nourmahnad, M. D. Smith, M. Zeller, G. M. Ferrence, J. Schrier and A. J. Norquist, *Inorg. Chem.*, 2015, **54**, 694-703.
37 Mathematica (version 10.0.0.0), Wolfram Research, Inc., Champaign, IL, 2014.
38 K. Momma, F. Izumi, *J Appl. Crystallogr.*, 2011, **44**, 1272-1276.
39 S. Krivovichev and P. Burns, *Mineral. Mag.*, 2000, **64**, 1069-1075.
40 M.-C. Corbeil and P. J. Sirois, *Stud. Conserv.*, 2007, **52**, 281-288.
41 H. Kim and K. Suslick, *Crystals*, 2018, **8**, 280–299.
42 S. K. Bhangu, M. Ashokkumar and J. Lee, *Cryst. Growth Des.*, 2016, **16**, 1934-1941.
43 B. Njegić Džakula, J. Kontrec, M. Ukrainczyk, S. Sviben and D. Kralj, *Cryst. Res. Technol.*, 2014, **49**, 244–256.
44 W. Kwestroo and C. Langereis, *J. Inorg. Nucl. Chem.*, 1965, **27**, 2533-2536.
45 C. H. Swanson, S. P. Cummings, M. Grysell, D. T. Tran, D. L. Rogow, A. G. Oliver and S. R. J. Oliver, *Dalton Trans.*, 2009, 9849-9853.
46 N. Brese and M. O'Keefe, *Acta Crystallogr.*, 1991, **B47**, 192-197.
47 S. Krivovichev and I. D. Brown, *Z. Kristallogr.*, 2001, **216**, 245-247.
48 R. L. Davidovich, V. Stavila, D. V. Marinin, E. I. Voit and K. H. Whitmire, *Coord. Chem. Rev*, 2009, **253**, 1316-1352.
49 T. Steiner, *Angew. Chem. Int. Ed.*, 2002, **41**, 48-76.
50 M. Nishio, Y. Umezawa, H. Suezawa and S. Tsuboyama, in *The Importance of Pi-Interactions in Crystal Engineering*, John Wiley & Sons, Ltd, Chichester, UK, 2012, ch. 2, pp. 1–39.
51 R. Bishop, in *The Importance of Pi-Interactions in Crystal Engineering*, John Wiley & Sons, Ltd, Chichester, UK, 2012, ch. 2, pp. 41–77.
52 L. Loots and L. J. Barbour, *CrystEngComm*, 2012, **14**, 300-304.
53 C. Janiak, *Dalton Trans.*, 2000, 3885-3896.
54 L. J. Fitzgerald and R. E. Gerkin, *Acta Cryst.*, 1993, **C49**, 1952-1958.
55 F. Zarekarizi and A. Morsali, *Inorg. Chem.*, 2020, **59**, 2988-2996.
56 P. Rönfeldt, H. Reinsch, M. P. M. Poschmann, H. Terraschke and N. Stock, *Cryst. Growth Des.*, 2020, **20**, 4686-4694.
57 M. Zhang, M. Bosch, T. Gentle III and H.-C. Zhou, *CrystEngComm*, 2014, **16**, 4069-4083.

The orientation of a ligand's bulk with respect to the coordinating group controls packing and symmetry in new lead oxide carboxylates.